PHYSICAL SCIENCES

STEM in situ thermal wave observations for investigating thermal diffusivity in nanoscale materials and devices

Hieu Duy Nguyen[1], Isamu Yamada[2], Toshiyuki Nishimura[3], Hong Pang[4], Hyunyong Cho[1], Dai-Ming Tang[4], Jun Kikkawa[1], Masanori Mitome[5], Dmitri Golberg[4,6,7], Koji Kimoto[1], Takao Mori[4,8], Naoyuki Kawamoto[1]*

Practical techniques to identify heat routes at the nanoscale are required for the thermal control of microelectronic, thermoelectric, and photonic devices. Nanoscale thermometry using various approaches has been extensively investigated, yet a reliable method has not been finalized. We developed an original technique using thermal waves induced by a pulsed convergent electron beam in a scanning transmission electron microscopy (STEM) mode at room temperature. By quantifying the relative phase delay at each irradiated position, we demonstrate the heat transport within various samples with a spatial resolution of ~10 nm and a temperature resolution of 0.01 K. Phonon-surface scatterings were quantitatively confirmed due to the suppression of thermal diffusivity. The phonon-grain boundary scatterings and ballistic phonon transport near the pulsed convergent electron beam were also visualized.

INTRODUCTION

More than half of electronic device failures are caused by heat-related factors (*1*). During operating and repeated on/off cycles over the lifetime, changes in the device's temperature lead to thermal fatigue, resulting in deformation, breaking, or cracking and, eventually, product failure. Therefore, thermal management is crucial for electronic devices across various industries. In addition, the development of microelectronic, thermoelectric, and photonic devices requires them to be smaller and more powerful, making thermal management a more critical issue than ever before. Furthermore, recent advances have reduced the size of these devices to be comparable to the phonon mean free path (MFP), pushing thermal transport to a regime where its behavior is different from that of bulk-sized counterparts (*2*, *3*). This substantial change complicates the issue and underscores the need for adequate thermal management at the nanoscale to prevent device failures. As a result, nanoscale spatial-resolved and precise thermometry is urgently required.

Many studies have aimed to characterize the thermal properties of nanostructures using well-known methods, such as time-domain thermal reflectance (TDTR) (*4*–*6*), transient Raman method (*7*, *8*), laser-assisted atom probe (*9*, *10*), atomic force microscopy–based thermometry using scanning thermal microscopy (SThM) (*11*–*13*), and scanning near-field optical microscopy (*14*, *15*). While SThM and near-field light adopting techniques are limited to surface measurement, TDTR and other methods using a laser as a heat source have challenges in achieving a spatial resolution of sub-10 nm. To enhance local heating capability, adopting an electron beam of a transmission electron microscope (TEM) as a nanosized heat source has been reported (*16*–*18*). So far, using the electron energy loss spectroscopy (EELS) technique, temperature mappings have been obtained by detecting the shifting of the plasmon peak (*19*), phonon peak (*20*), and the ratio between the intensity of gain and loss peaks (*21*, *22*). This approach yields excellent spatial resolution without affecting the specimen. However, even with the outstanding energy resolution of sub-10 meV, there is still a deviation of several to tens of degrees in the measurement precision (*21*). Furthermore, generating a thermal gradient is essential, making it challenging to characterize thermosensitive materials. Instead of detecting temperature via changes in other physical properties, in our previous studies, we directly measured a subtle temperature change induced by the electron beam in a TEM using a nanosized thermocouple (*23*, *24*). However, according to Fourier's law, determining local temperatures requires knowing specimen thickness, which complicates the measurements.

Here, we report a method using a pulsed convergent electron beam under a scanning transmission electron microscopy (STEM) mode in a TEM to heat microfabricated specimens and measure the phase delay and amplitude of thermal waves induced by the pulsed focused electron beam at room temperature (RT). The fundamental theory of this study is described in the Supplementary Materials. In short, a single-crystalline sapphire specimen was used as a one-dimensional thermal conductor. An electrostatic dose modulator (EDM) periodically blanked the electron beam at a rate of up to 100 kHz to produce a periodic heat source. The phase delay and amplitude of thermal waves at each position irradiated by the pulsed focused electron beam were acquired by a lock-in amplifier. In STEM mode, the pulsed convergent electron beam was scanned pixel by pixel across a desired image frame, allowing for the simultaneous acquisition of a high-angle annular dark-field scanning transmission electron microscopy (HAADF-STEM) image and a map of the phase delay or amplitude of thermal

---

[1]Center for Basic Research on Materials, National Institute for Materials Science, 1-1 Namiki, Tsukuba, Ibaraki 305-0044, Japan. [2]Yamada R&D Support Enterprise, 2-8-3 Minamidai, Ishioka, Ibaraki 315-0035, Japan. [3]Research Center for Structural Materials, National Institute for Materials Science, 1-2-1 Sengen, Tsukuba, Ibaraki 305-0047, Japan. [4]Research Center for Materials Nanoarchitectonics, National Institute for Materials Science, 1-1 Namiki, Tsukuba, Ibaraki 305-0044, Japan. [5]Research Network and Facility Services Division, National Institute for Materials Science, 1-2-1 Sengen, Tsukuba, Ibaraki 305-0047, Japan. [6]Centre for Materials Science, Queensland University of Technology, 2 George, Brisbane, QLD 4000, Australia. [7]School of Chemistry and Physics, Faculty of Science, Queensland University of Technology, 2 George, Brisbane, QLD 4000, Australia. [8]Graduate School of Pure and Applied Sciences, University of Tsukuba, Tennodai 1-1-1, Tsukuba 305-8671, Japan.
*Corresponding author. Email: kawamoto.naoyuki@nims.go.jp

waves (Fig. 1). In addition, a polycrystalline aluminium nitride (AlN) specimen was prepared using the same method as for the single-crystalline sapphire specimen to investigate the thermal transport of thermal waves at local areas, including grain boundaries.

RESULTS

Thermal waves induced by the pulsed focused electron beam

A pulsed convergent electron beam in STEM mode is scanned across the specimen. It is considered that the heat induced by the electron beam dissipates along the length of the specimen toward both ends. The whole experimental system is kept inside a TEM column at a high vacuum (~2×10^{-5} Pa) at RT; as a result, both radiation and convection are considered to be negligible. A thermocouple is formed by contacting two nanosized tips, and the other ends are fixed to two movable Cu hats attached to the TEM holder (fig. S1) to detect temperature. The reference temperature is designed to be inside the TEM column, which is sufficiently stable for the measurement and equivalent to RT. For each scanning, a HAADF-STEM image and a corresponding map of phase delay are simultaneously acquired, as shown in Fig. 1 (C and D). The map of phase delay shows a gradient with respect to the phase-locked position (marked by a black cross in Fig. 1D). When the electron beam is irradiated on the thermocouple, a sudden change of phase delay is observed due to the thermal contact resistance between the thermocouple and the specimen. Conversely, nothing is heated when the electron beam is emitted in a vacuum, and the phase delay cannot be detected. Any acquired signal in this area should be considered as noise.

The propagation of thermal waves within the single-crystalline sapphire specimen was monitored by an oscilloscope. Figure 2B shows the signal waveform of the EDM and the corresponding electron beam–induced thermal wave when the electron beam is irradiated on the red cross marked in Fig. 2A. The waveform exhibits separate heating and cooling periods, as observed in Fig. 2B. During the heating period, there is a sharp increase in thermal electromotive force (or temperature) of approximately 0.7 ms, followed by a relatively uniform plateau in the remaining period of about 0.8 ms. The temperature remarkably decreases over only 0.7 ms during the cooling period. At low modulated frequencies, the thermal wave starts and ends each cycle at zero level (RT), indicating that thermal decay is complete in each cycle. At higher modulated frequencies, the thermal wave does not have enough time for relaxation, resulting in fluctuating around a temperature

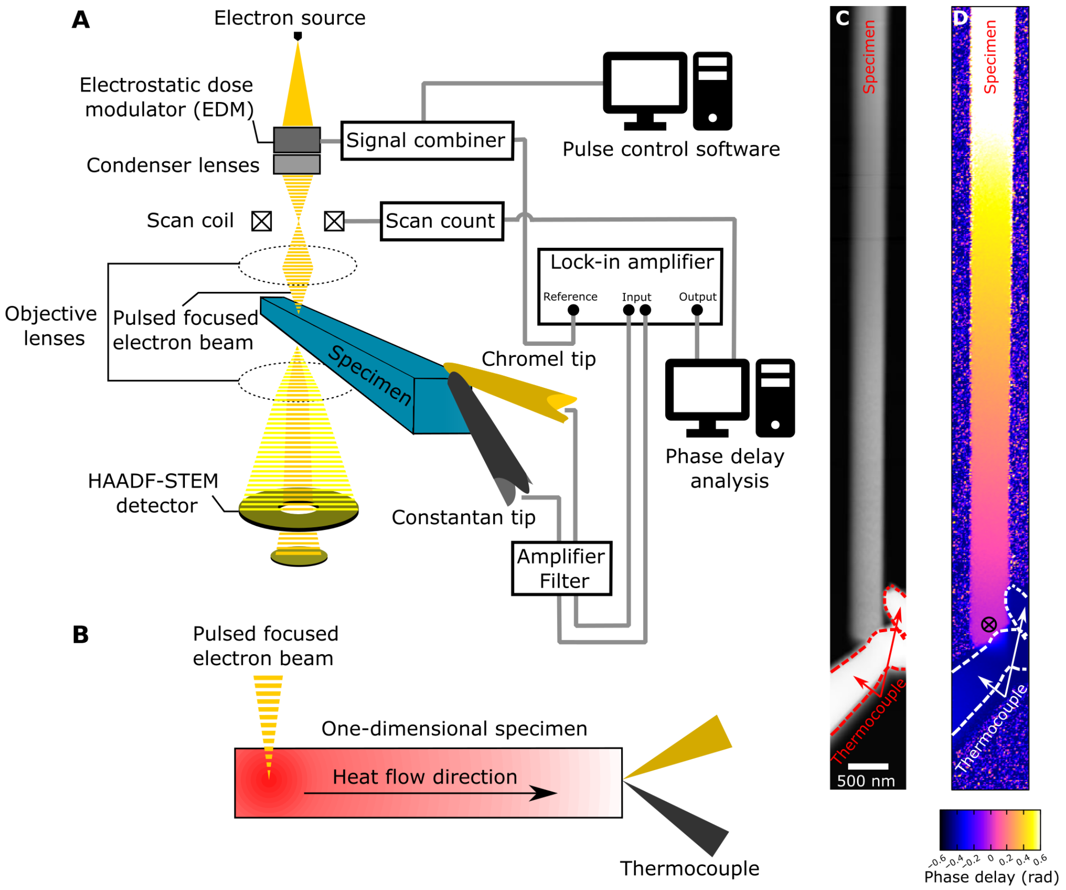

Fig. 1. Experiment overview. (**A**) Apparatus: A TEM, an EDM for generation of the pulsed focused electron beam, a two-probe scanning tunneling microscopy–TEM holder equipped with constantan and chromel piezo-driven probes, and a lock-in amplifier accompanied by a data analysis system. (**B**) Description of heat flow in a one-dimensional specimen used in the present study. (**C**) Low-magnification HAADF-STEM image of the experimental setup. (**D**) Map of phase delay corresponding to the area of (C). The cross mark near the tip of the specimen indicates the position where the phase was selected to be zero.

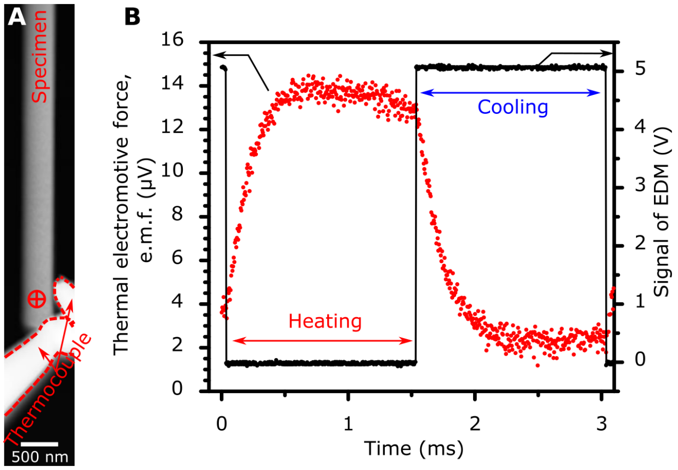

Fig. 2. Waveforms of pulsed-focused electron beam–induced thermal wave. (**A**) HAADF-STEM image of experimental setup using the single-crystalline sapphire specimen. (**B**) The waveform of signal controlled by EDM (black) and that of thermal electromotive force yielded by the nanosized thermocouples (red). The measured position is shown by the red cross mark in (A).

level attained immediately after the electron beam irradiation (fig. S2). This temperature level is the extent of temperature increase above RT. Consequently, all measurements were carried out after the temperature of the specimen became stable. The dependence of thermal waves on thermocouples is discussed in the Supplementary Materials.

Thermal waves in a one-dimensional single-crystalline sapphire specimen

On the basis of Eq. 5, the gradient of phase delay allows us to determine the thermal diffusivity value for a known modulated frequency. Figure 3A shows a HAADF-STEM image of the single-crystalline specimen and maps of phase delay under modulated frequencies of 5, 10, and 20 kHz. The gradients of phase delay are observed to correlate with the modulated frequencies of the pulsed convergent electron beam. It is important to note that the data of phase delay are recorded on the basis of the difference in phase of thermal waves between the irradiated positions and the phase-locked position which is selected close to the contact of the specimen and the thermocouple, as shown in Fig. 1D. In Fig. 3A (2 to 4), five line profiles were taken in each case of modulated frequency. The results of the representative line profiles are depicted in Fig. 3B, where all the line profiles are well-fitted by a linear approximation. The slopes of the linear best fits enable us to determine the thermal diffusivity values using Eq. 5. It is essential to clarify that the response time of thermal waves remains unchanged when the electron beam is scanned (fig. S4). Therefore, the phase delay obtained by the lock-in amplifier must be correct throughout the investigated area.

Figure 3C shows the results with error bars indicating uncertainties. A deviation of ~4% within these results compared to the average value of 6.87×10^{-6} m^2/s indicates an acceptable result for a quantitative measurement. The determined thermal diffusivity values are approximately 0.64 times the reference data (*25*–*27*) and the measured bulk thermal diffusivity of sapphire (Supplementary Materials). It is worth mentioning that inevitable amorphization and lattice distortion due to focused Ga-ion beam microfabrication might negatively affect the thermal diffusivity of the specimen. However, this effect should be minor considering parallel model of effective thermal diffusivity (Supplementary Materials). The reduction in thermal diffusivity is consistent with the thermal conductivity reduction observed when the characteristic length of thermal transport material is reduced to approximately 400 nm in a recently reported study adopting time-domain thermoreflectance conducted at RT (*28*). Theoretical and empirical studies have described the reduction of thermal conductivity by classical (Casimir) size effect (*29*) or phonon spectral distribution (*30*). According to these studies, phonons with different MFPs contribute dissimilarly to the thermal conductivity of a material. When the width and thickness of the specimen become much smaller than the bulk phonon MFPs, this leads to the suppression of the thermal conductivity. The physics of phonons, in this case, has been commonly acknowledged to follow the natures in the ballistic regime (*31*–*33*). In addition, the thermal (*34*) and electron beam (*35*) excitation may induce the surface phonon polaritons (SPhPs) on the specimen. The contribution of SPhPs increases and enhances the in-plane thermal conductivity with decreasing film thickness, especially below 200 nm (*36*, *37*). In the present study, since the thickness of the specimen is in a range of several hundred nanometers, the contribution of SPhPs to thermal conductivity can be considered negligible.

The amplitude of thermal waves provides information on the combined effects of absorbed thermal energy, density, specific heat, and thermal diffusivity. Figure 3A (5 to 7) shows maps of amplitude with modulated frequencies of 5, 10, and 20 kHz, with the amplitude decreasing as the distance from the detecting point increases. Line profiles along C_1D_1, C_2D_2, and C_3D_3 are shown in Fig. 3D, which are taken at the center of each image. Uneven slopes at positions 3 μm and 6 to 8 μm are attributed to imperfections on the specimen's surface, likely damages caused by the Ga-ion beam of focused ion beam (FIB). It is worth noting that these imperfections are not revealed in energy dispersive spectroscopy (EDS) elemental maps in fig. S1 or the HAADF-STEM image at the current magnification. With the experimental setup used, the input signal should include nothing except thermal waves induced by the pulsed convergent electron beam. Therefore, the amplitude of thermal waves has the potential to provide detailed information about the surface structures and compositions of materials.

In this study, using a nanosized thermocouple yielded uninterrupted experimental data, we prove that the sensitivity of the thermocouple is high enough to detect fine amplitudes of thermal waves. The sensitivity of the lock-in amplifier was also adjusted to ensure that it was high enough to detect delicate signals of thermal waves without overloading. With these adjustments, the amplitude can be detected with an accuracy of three significant numbers. As a result, assuming that the Seebeck coefficient is constant, the smallest distinguishable temperature difference is estimated to be 0.01 K at RT, which is believed to be one of the best temperature resolutions achieved among various nanoscale thermometry methods [temperature resolutions of 7 to 15 mK and several to a few tens of Kelvin were reported using SThM (*11*–*13*) and EELS-based method (*19*–*22*), respectively]. Calculated data using Eq. 6 exhibits an acceptably consistent trend with experimental data at the corresponding distance. The divergence is attributed to imperfections in the specimen, such as differences in thickness,

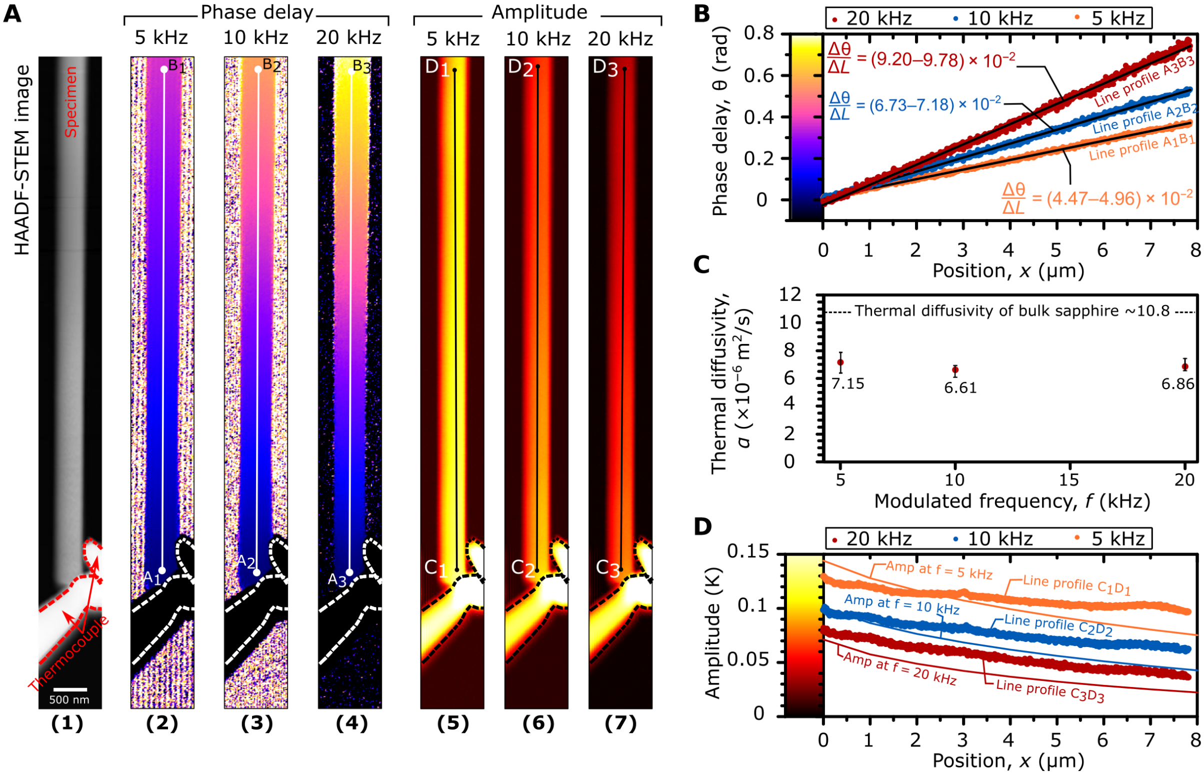

Fig. 3. Characterization of phase delay and amplitude of thermal waves in a one-dimensional single-crystalline sapphire specimen. (**A**) (1) HAADF-STEM image of the experimental setup, (2 to 4) maps of phase delay, and (5 to 7) maps of amplitude adopting pulsed electron beam at modulated frequencies of 5, 10, and 20 kHz, respectively. Five lines in each case of modulated frequency were drawn to characterize line profiles, among which A_1B_1, A_2B_2, A_3B_3, and C_1D_1, C_2D_2, and C_3D_3 show representative lines along which gradients of phase delay and amplitude were investigated for frequencies of 5, 10, and 20 kHz, respectively. (**B**) Line profiles and best fits along A_1B_1, A_2B_2, and A_3B_3 in (A) and gradients of phase delay. Note that the ranges of gradient indicate the uncertainties of the measurements. (**C**) Thermal diffusivity is calculated from obtained gradients of phase delay in various modulated frequencies. The thermal diffusivity of bulk sapphire along the *a* axis was estimated to compare with the reduced thermal diffusivity due to phonon scattering at the surfaces of the specimen whose width and thickness are smaller than the phonon MFP of sapphire. (**D**) Line profiles along C_1D_1, C_2D_2, and C_3D_3 of map of amplitude and amplitude calculated using Eq. 6. Empirically acquired amplitudes of thermal waves exhibit an acceptable consistency with theoretical calculations.

surface conditions, and Ga-ion beam-induced surface damages, which result in the nonuniformity of the absorbed thermal energy. The presence of Ga also affects the effective thermal diffusivity of the specimen, resulting in divergence from the assumption of a homogeneous single-crystalline sapphire specimen.

Thermal waves in a two-dimensional polycrystalline AlN specimen

In practical applications, materials often contain numerous defects, such as grain boundaries, voids, and dislocations, which make the local thermal properties more complex. In this study, a polycrystalline AlN specimen was prepared to investigate the local thermal measurement by detecting the phase delay and amplitude of thermal waves induced by a pulsed focused electron beam. As a part of a sintered body, the polycrystalline AlN specimen is expected to contain grain boundaries, voids, and other defects. To visualize the thermal properties of such nanoscale structures, a modulated frequency of 100 kHz was used. Figure 4A shows a HAADF-STEM image of the microfabricated TEM specimen of the polycrystalline AlN contacted with a thermocouple for thermal measurements. Two smaller areas surrounded by dashed lines (1) and (2) are enlarged on the right side. Corresponding to the enlargement of area (1), a map of the phase delay of this area was acquired. Like the single-crystalline sapphire specimen, the phase-locked (or zero-phase–selected) position is close to the contact between the thermocouple and the specimen.

First, the map of phase delay in this area discloses that the phase delay increases with increasing the distance from the zero-phase–selected position. A stronger contrast is visible in the vicinity of grain boundaries. This result implies that the thermal waves induced by pulsed focused electron beam irradiated onto these grain boundaries spend more time arriving at the specimen-thermocouple junction, which is attributed to more considerable thermal resistance. The grain boundaries themselves have been known to obstruct the propagation of thermal waves and have been used to suppress thermal conductivity to enhance the performance of thermoelectric materials (*38*). At these grain boundaries, phonons, prominent heat transport carriers in semiconductor materials like AlN, are scattered, leading to the reduction of thermal conductivity (*39*, *40*). Particularly, AlN is known to hinge on strong phonon-boundary scattering effects due to the large phonon MFPs, which is discernible even in sub–10-μm thin films (*41*–*43*). Numerical calculation estimates that half of the AlN bulk thermal conductivity is contributed by phonons with MFPs

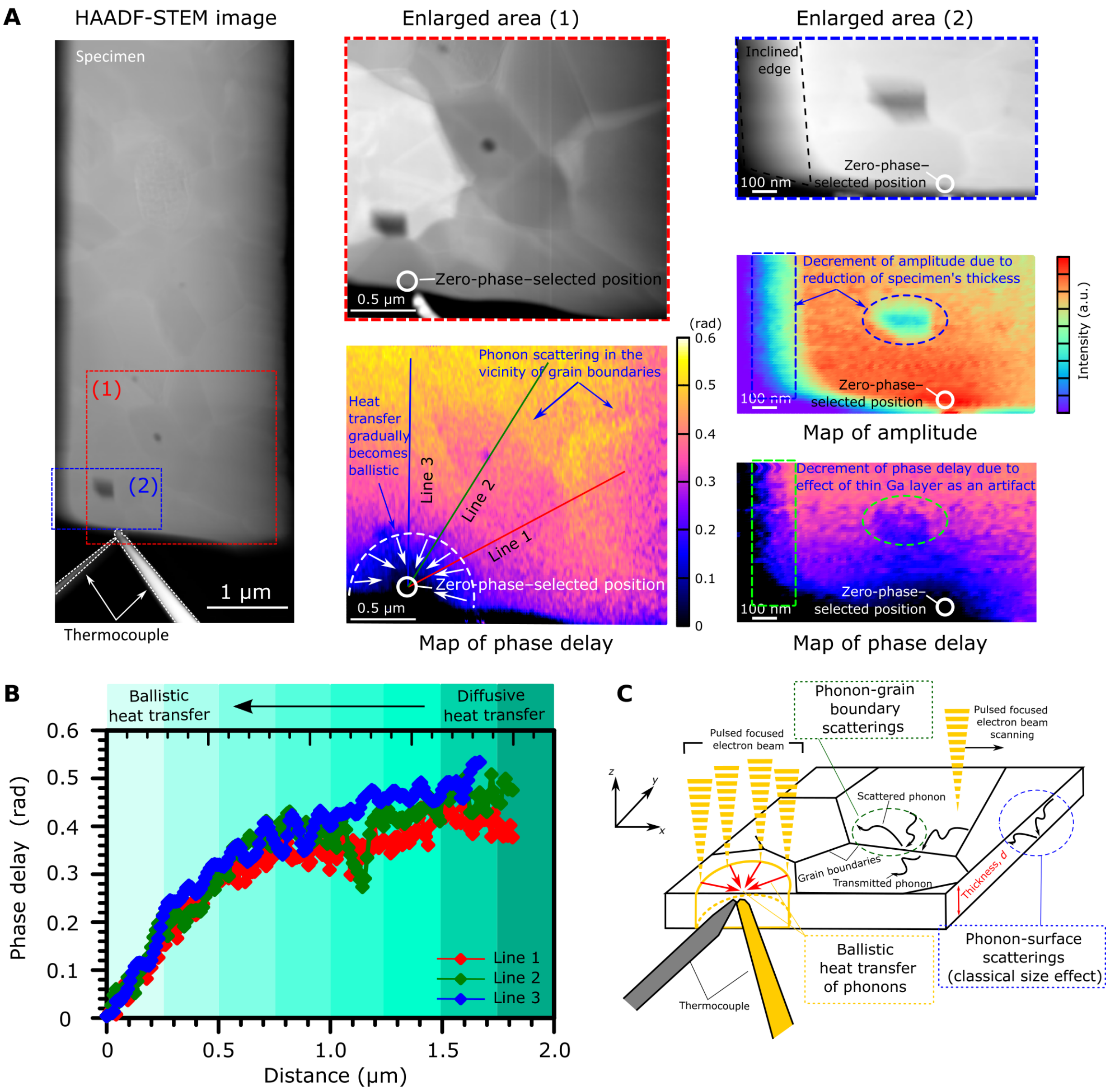

Fig. 4. Characterization of the phase delay and amplitude of the thermal waves in a two-dimensional polycrystalline AlN specimen. (**A**) HAADF-STEM image of polycrystalline AlN specimen and two enlarged areas where phase delay and amplitude of the thermal waves were obtained. Phonon scatterings in the vicinity of grain boundaries are visualized via a stronger contrast of phase delay in the area (1), indicating the thermal resistance of these grain boundaries. Changes in phase delay and amplitude at intergranular pores are visualized in areas (1) and (2). Three lines are drawn on a map of phase delay in area (1). Profiles along these lines are shown in (**B**). The steep gradient of phase delay at the area close to the thermocouple junction indicates an exceptional diminution of thermal diffusivity, which implies ballistic heat transfer. (**C**) Mechanism demonstration image shows possible phonon scattering events and ballistic heat transfer within the thermal measurements in the present study. a.u., arbitrary units.

larger than 300 nm at RT (*44*). In addition, image analysis shows that phase-spatial resolution attains ~10 nm. A better resolution can be obtained by optimizing measurement's conditions (see the Supplementary Materials). Therefore, the observations of phonon-grain boundary scatterings of AlN in the current specimen are reasonable.

Line profiles in Fig. 4B show a substantial plunge of phase delay inside the area in the range of approximately 400 nm from the specimen-thermocouple junction. This steep decrement refers to a further reduction of thermal diffusivity. The closer the electron beam approaches the thermocouple, the larger the Knudsen number (the ratio between phonon MFP and characteristic length) becomes (*32*). On the other hand, the heat source (pulsed convergent electron beam) is much smaller than phonon MFPs (*45*). Calculating the ballistic thermal resistance near an electron beam using the Boltzmann transport equation indicates that the ballistic effects are localized near the heated region while the thermal transport far from the origin is well described by the diffusive mechanism of Fourier's law (*46*). Therefore, this result suggests the continuous transformation of heat transfer from a diffusive to a ballistic regime. The effects of voids on phase delay and amplitude of thermal waves are discussed in the Supplementary Materials.

Qualitatively, the phase delay obtained in these results can demonstrate how fast the thermal waves induced by the pulsed convergent electron beam arrive at the specimen-thermocouple junction. This visualization is favorable for heat path investigation and thermal management of materials and devices with micro/nanostructures. In the scope of the present study, we refrain from determining the thermal diffusivity of polycrystalline AlN specimen quantitatively (as for the case of single-crystalline sapphire specimen) because of the complexity of two-dimensional grain boundaries, which may complicate the physics and need further studies to clarify.

DISCUSSION

Because of the subtle heating effect of the electron beam, the nanosized thermocouple is considered the critical factor in detecting the small thermal wave induced by the pulsed focused electron beam. While a thermocouple with too-large tips cannot detect small signals due to immense heat capacity, a thermocouple with too-small tips confronts difficulty in stable contact with the specimen. Therefore, a thermocouple with an appropriate size is crucial. In addition, the surface of the tips should be sufficiently clean for both effective thermal contact with the specimen and electrical contact with each other. On the other hand, if absolute values of the amplitude of thermal waves are required, then the variation of the Seebeck coefficient due to the size effect should be considered (*47–50*). This phenomenon occurs when the characteristic size becomes smaller than the MFP of electrons inside the metals (*51*). The MFP of electrons inside chromel and constantan was determined to be ~37 and ~100 nm, respectively. Although the variation of the Seebeck coefficient has not been confirmed in our experiments, attention should be paid when using any thermocouple whose size is less than the MFP of electrons of either constituent metal.

The phase-spatial resolution of the method we report here strongly depends on the frequency modulated by the electron beam blanking system and the phase resolution of the lock-in amplifier. According to Eq. 5, phase delay per distance is proportional to the square root of modulated frequency. As the phase resolution of the lock-in amplifier is constant, increasing the modulated frequency helps to enhance the spatial resolution of the map of phase delay (movies S1 to S3). Unfortunately, thermal waves attenuate with increasing the distance by an exponential function where the modulated frequency gets involved, as shown in Eq. 4. As a result, adjusting modulated frequency is a trade-off between the spatial resolution of the map of phase delay and the intensity (or accuracy) of the detected phase delay and amplitude. In addition, the thermal diffusivity of the examining specimen also affects the phase-spatial resolution. According to Eq. 5, materials having large thermal diffusivity should require higher modulated frequency and vice versa. Here, we were able to carry out thermal measurements up to 100 kHz. Thermally highly conductive materials such as metals and some metallic alloys with thermal diffusivity in the range of ~10^{-5} to ~10^{-4} m^2/s may require higher modulated frequency to visualize delicate structures, while less thermally conductive materials such as amorphous materials (glass, plastics, etc.) with thermal diffusivity in the range of ~10^{-7} m^2/s require a lower modulated frequency. Using a thicker specimen or an electron beam with a lower acceleration voltage is also a way to magnify the heating effect of the electron beam. Generally speaking, specific technical factors are expected to be tuned appropriately for a particular specimen. More details concerning phase-spatial resolution are mentioned in the Supplementary Materials.

Summarily, in the present study, we demonstrated a STEM-based in situ method to record the phase delay and amplitude of the electron beam–induced thermal waves propagating along FIB-microfabricated single-crystalline sapphire and polycrystalline AlN specimens. By characterizing the phase delay and the amplitude of thermal waves, we succeeded in determining the effective thermal diffusivity of the single-crystalline sapphire specimen and visualizing the phonon-grain boundary scatterings in the vicinity of grain boundaries in the polycrystalline AlN specimen. In this way, we can confirm the suppression of thermal diffusivity due to the classical size effect (Casimir size effect). In addition, the visualization of phase delay by exact local heating with beam size smaller than phonon MFPs of most of the materials at RT provides a promising method to study ballistic phonon transport in micro/nanostructures. The feasibility of measuring at RT (without heating to generate a thermal gradient) paves the way to characterize heat-sensitive materials. With unprecedented spatial and temperature resolution, the method reported here is expected to facilitate troubleshooting or designing electronic, photonic, and thermoelectric devices with better thermal management to avoid failure due to thermal issues. Further studies adopting the present method will be carried out for various materials to unravel the thermal properties of newly discovered micro-/nanomaterials for future multifunctional devices.

MATERIALS AND METHODS

Theoretical calculation of phase delay and amplitude of thermal waves

The present study is based on a periodic heating method pioneered by Angstrom for thermal conductivity measurement (*52*). This method involves periodic heating of one end of a one-dimensional thermal conductor and measuring the phase delay of thermal waves at a specific distance from that end to directly determine the thermal diffusivity and conductivity of the thermal conductor. Notably, it does not require prior knowledge of the specimen thickness. In our experimental setup, as shown in Fig. 1, there is no temperature gradient along the specimen width, allowing us to apply a one-dimensional heat transport equation as follows

$$\frac{\mathrm{d}^2 T(x,t)}{\mathrm{d}x^2} = \frac{1}{\alpha}\frac{\mathrm{d}T(x,t)}{\mathrm{d}t} \tag{1}$$

where T is the temperature, α is the thermal diffusivity, x is the distance, and t is the time. The whole experimental system is kept inside a TEM column at a high vacuum (~2×10^{-5} Pa); as a result, heat dissipated from the specimen into the surrounding environment could be neglected. In addition, as the experiments are carried out at RT, thermal radiation should be negligibly small. The periodic heat source is generated by an electron beam blanking system using a square pulse train with modulated frequencies of 0.3 to 100 kHz. The electron beam provides the specimen with a heat flux of $Q(t)$. $Q(t) = Q_0$ when the beam is exposed and $Q(t) = 0$ when the beam is blanked. As the switching time was less than 20 ns, a square pulse waveform almost remains constant. The Fourier transform can be derived as follows (*53*)

$$Q(t) = Q_0\left[\frac{1}{2} + \sum_{\substack{n=-\infty \\ n\neq 0}}^{\infty}\left|\frac{\sin\left(\frac{n\pi}{2}\right)}{n\pi}\right| \cdot \exp\left\{i\left(n\omega t - \frac{n\pi}{2}\right)\right\}\right] \tag{2}$$

Note that a duty cycle of 50% is used throughout the present study. In addition, Q_0 is the total heat flux generated inside the specimen using a convergent electron beam without modulating and identified by

$$Q_0 = \frac{1}{A} \times P = \frac{1}{A} \times \left(\frac{\pi r_0^2 J}{e}\frac{\Delta E}{\Lambda}\mathrm{t}\right) \tag{3}$$

where A is the cross-sectional area of the specimen, P is the power of heating effect on the specimen induced by the electron (*54*) with an assumption that only plasmon energy loss ΔE with an electron MFP Λ contributes to the heat generation, r_0 is the radius of the electron beam, J is the current density of the electron beam, e is the elementary charge, $\Delta E = 24$ eV is the plasmon energy loss of sapphire, $\Lambda = 143$ nm is the electron MFP of sapphire at an acceleration voltage of 300 kV (*55*), and d is the specimen thickness. Here, the current of electron beam $I = \pi r_0^2$ is 0.5 nA with standard settings (Figs. 1 to 3 and fig. S3) and 1.4 nA with beam current–enhanced settings (Fig. 4 and figs. S2 and S4). The current of the electron beam was measured via a Faraday cup. In addition, the specimen was fabricated from a single-crystalline sapphire bulk with relatively uniform width and thickness. Therefore, Q_0 could be considered relatively constant along the length of the specimen. Solving Eq. 1 for each nth order and assuming a linear summation of thermal waves (*53*), we have

$$T(x,t) = \frac{Q_0}{\rho C_p\sqrt{\alpha}}\sum_{\substack{n=-\infty \\ n\neq 0}}^{\infty}\left|\frac{\sin\left(\frac{n\pi}{2}\right)}{n\pi}\right|\sqrt{\frac{1}{2|n|\pi f}}\exp\left(-\sqrt{\frac{|n|\pi f}{\alpha}}x\right)\exp\left[i\left(n\omega t - \sqrt{\frac{|n|\pi f}{\alpha}}x - \frac{\pi}{4} - \frac{n\pi}{2}\right)\right] \tag{4}$$

where ρ is the density, and C_p is the specific heat capacity. The solution is expressed as a complex number in which the modulus is the amplitude and the argument is the phase of the thermal wave. Note that the difference in phase delay allows us to determine the thermal diffusivity of the specimen directly. Without loss of generality and considering the difference in phase delay of first order of thermal waves at two separate positions, we have

$$\Delta\theta = \theta_1 - \theta_2 = \sqrt{\frac{\pi f}{\alpha}}(x_2 - x_1) \tag{5}$$

where θ_1 and θ_2 are the phase delays of thermal waves measured at distances x_1 and x_2 from a specific position, respectively. Throughout this study, this position is selected to be a point close to the thermal junction between the specimen and thermocouple. Similarly, the amplitude of the thermal wave with respect to distance is indicated by

$$\mathrm{Amp}(x) = \frac{Q_0}{\rho C_p\sqrt{\alpha}}\sum_{\substack{n=-\infty \\ n\neq 0}}^{\infty}\left|\frac{\sin\left(\frac{n\pi}{2}\right)}{n\pi}\right|\sqrt{\frac{1}{2|n|\pi f}}\exp\left(-\sqrt{\frac{|n|\pi f}{\alpha}}x\right) \tag{6}$$

In this study, a single-crystalline sapphire specimen was used as the heat conductor. This specimen was fabricated using a FIB, with its length direction perpendicular to the c axis of the sapphire unit cell. A nanosized chromel-constantan thermocouple (type E) was firmly placed at one end of the specimen, while the other end was fixed to the TEM holder (refer to fig. S1). An EDM periodically blanked the electron beam at a modulated frequency of up to 100 kHz to produce a periodic heat source. The phase delay and amplitude of thermal waves at each position irradiated by the pulsed electron beam were acquired by a lock-in amplifier. Note that the lock-in amplifier indicates the root mean square value of the AC thermal waves. In STEM mode, the pulsed convergent electron beam was scanned pixel by pixel across a desired image frame, allowing for the simultaneous acquisition of an HAADF-STEM image and a map of the phase delay or amplitude of thermal waves (see Fig. 1). In addition to the single-crystalline sapphire specimen, a polycrystalline AlN specimen was prepared using the same method as the single-crystalline sapphire specimen to investigate the thermal transport of thermal waves at local areas, including grain boundaries.

Hardware

Electron microscopy data were acquired using a JEOL JEM-3100FEF TEM, operating at an acceleration voltage of 300 kV and equipped with an electrostatic dose modulation (EDM Basic) system manufactured by JEOL to generate a pulsed electron beam. The electron beam was controlled in STEM mode, with a condenser lens aperture of 70 μm, beam convergence semi-angle of ~6.8 mrad, effective beam size of about 2 to 3 nm, and exposing beam current of ~0.5 nA under standard settings (Figs. 1 to 3 and fig. S3) and ~1.4 nA under beam current–enhanced settings (Fig. 4 and figs. S2 and S4). Beam scanning in STEM mode was controlled using a Gatan DigiScan system. To maximize the amplitude of AC thermal waves, the electron beam was modulated with a duty cycle of 50% under all conditions. The maximum modulated frequency of EDM at an acceleration voltage of 300 kV was 500 kHz. An in situ heating experiment was conducted using a twin-probe scanning tunneling microscopy–TEM holder manufactured by "Nanofactory Instrument AB" (fig. S1) (*23*, *24*). Nanosized chromel and constantan tips were used as thermocouples for precise temperature detection and were fabricated by electrochemical etching of chromel and constantan wires with a diameter of 200 μm [for details, see (*56*)]. The reference junction temperature for calibration of the thermocouple was the temperature of the Cu jigs holding the chromel and constantan probes (see fig. S1), which was always kept at ~298 K (RT) inside the TEM column. Because of the heat capacity of both metallic wires and the large heat capacity of Cu jigs, supporting sapphire balls, and metal rods of the TEM holder, the reference temperature should not be affected by a temperature increase (within at least several 10 K) with respect to the nanosized junction.

The chromel and constantan probes were independently approached and delicately physically contacted to the specimen by a piezo-driving system. The electrical resistance of the junction was carefully checked by passing a 100-nA dc through two probes and measuring the induced voltage. The whole impedance of the electrical circuit, including the thermocouple and its junction, is considered predominant and needs to be less than or equal to 1 kilohm (to yield sufficiently clear signals of oscillating thermal waves). To acquire the phase delay and amplitude of thermal waves during the electron beam scanning process and monitoring signals, respectively, a lock-in amplifier (model SR865A, Stanford Research Systems) was used in conjunction with an oscilloscope (Keysight InfiniiVision DSOX3034T). The time constant and sensitivity were adjusted to achieve an acceptable signal-to-noise ratio. The sensitivity was also adjusted to detect subtle signals of thermal waves but was low enough not to get overloaded. In addition, the exposure time for one pixel was adjusted to be equal to or longer than the time constant to ensure that the map of phase delay or amplitude would not be shifted with respect to the HAADF-STEM image. Noise-canceling filters and differential amplifiers were used to extract unexpected environmental noise and enlarge desirable signals, respectively. To avoid the drifting of the specimen (stage), each measurement was accomplished within 2 hours, taking into consideration the exposure time and the number of pixels for scanning, so that the deformation of the map of phase delay and amplitude would not occur.

The measurement of bulk thermal diffusivity along *c* axis of single-crystalline sapphire was carried out by a laser flash system (Netzsch LFA 467, Germany) at RT. The average value after three times measuring is 1.1595×10^{-5} m^2/s. The bulk thermal diffusivity along the *c* axis and *a* axis of single-crystalline sapphire at RT was calculated to be 1.1363×10^{-5} and 1.0635×10^{-5} m^2/s, respectively [using data in (*26*, *27*)]. The bulk thermal diffusivity along *a* axis of the single-crystalline sapphire specimen adopted in the present study is estimated to be ~1.0852×10^{-5} m^2/s (Fig. 3C).

Specimens

The specimen of single-crystalline sapphire was prepared from a commercial sapphire C-plane single-crystal substrate using a FIB system (Hitachi-FB2000). The specimen of polycrystalline AlN was microfabricated using a FIB system (Hitachi Ethos NX-5000). The bulk sample of AlN was synthesized using spark plasma sintering of high-purity AlN powder (grade E, Tokuyama Corporation) in the N_2 atmosphere. The grain size is observed in the range between 0.5 and 1 μm. Following microfabrication, each specimen was attached to a constantan tip by a W deposition inside the FIB system and then placed on a Cu attachment for stabilizing with the TEM holder (refer to fig. S1). The single-crystalline sapphire specimen has dimensions of ~20 μm (length) by ~430 nm (width) by ~430 nm (thickness), and the polycrystalline AlN specimen has dimensions of ~20 μm (length) by ~2.8 μm (width) by ~200 to 350 nm (thickness).

Supplementary Materials

This PDF file includes:
Supplementary Text
Figs. S1 to S7
Legends for movies S1 to S3
References

Other Supplementary Material for this manuscript includes the following:
Movies S1 to S3

REFERENCES AND NOTES

1. Dave S. Steinberg, Preface in Ed. 3, *Vibration Analysis For Electronic Equipment* (Wiley-Interscience, ed. 3, 2000).
2. I. Ferain, C. A. Colinge, J.-P. Colinge, Multigate transistors as the future of classical metal–oxide–semiconductor field-effect transistors. *Nature* **479**, 310–316 (2011).
3. X.-L. Shi, J. Zou, Z.-G. Chen, Advanced thermoelectric design: From materials and structures to devices. *Chem. Rev.* **120**, 7399–7515 (2020).
4. R. Anufriev, J. Ordonez-Miranda, M. Nomura, Measurement of the phonon mean free path spectrum in silicon membranes at different temperatures using arrays of nanoslits. *Phys. Rev. B* **101**, 115301 (2020).
5. K. M. Hoogeboom-Pot, J. N. Hernandez-Charpak, X. Gu, T. D. Frazer, E. H. Anderson, W. Chao, R. W. Falcone, R. Yang, M. M. Murnane, H. C. Kapteyn, D. Nardi, A new regime of nanoscale thermal transport: Collective diffusion increases dissipation efficiency. *Proc. Natl. Acad. Sci. U.S.A.* **112**, 4846–4851 (2015).
6. A. Sood, R. Cheaito, T. Bai, H. Kwon, Y. Wang, C. Li, L. Yates, T. Bougher, S. Graham, M. Asheghi, M. Goorsky, K. E. Goodson, Direct visualization of thermal conductivity suppression due to enhanced phonon scattering near individual grain boundaries. *Nano Lett.* **18**, 3466–3472 (2018).
7. J. Liu, H. Wang, Y. Hu, W. Ma, X. Zhang, Laser flash-Raman spectroscopy method for the measurement of the thermal properties of micro/nano wires. *Rev. Sci. Instrum.* **86**, 014901 (2014).
8. C. Li, S. Xu, Y. Yue, B. Yang, X. Wang, Thermal characterization of carbon nanotube fiber by time-domain differential Raman. *Carbon* **103**, 101–108 (2016).
9. L. Arnoldi, M. Spies, J. Houard, I. Blum, A. Etienne, R. Ismagilov, A. Obraztsov, A. Vella, Thermal diffusivity of diamond nanowires studied by laser assisted atom probe tomography. *Appl. Phys. Lett.* **112**, 143104 (2018).
10. A. Kumar, J. Bogdanowicz, J. Demeulemeester, J. Bran, D. Melkonyan, C. Fleischmann, W. Vandervorst, Measurement of the apex temperature of a nanoscale semiconducting field emitter illuminated by a femtosecond pulsed laser. *J. Appl. Phys.* **124**, 245105 (2018).
11. K. Kim, W. Jeong, W. Lee, P. Reddy, Ultra-high vacuum scanning thermal microscopy for nanometer resolution quantitative thermometry. *ACS Nano* **6**, 4248–4257 (2012).
12. F. Menges, P. Mensch, H. Schmid, H. Riel, A. Stemmer, B. Gotsmann, Temperature mapping of operating nanoscale devices by scanning probe thermometry. *Nat. Commun.* **7**, 10874 (2016).
13. S. Gonzalez-Munoz, K. Agarwal, E. G. Castanon, Z. R. Kudrynskyi, Z. D. Kovalyuk, J. Spièce, O. Kazakova, A. Patanè, O. V. Kolosov, Direct measurements of anisotropic thermal transport in γ-InSe nanolayers via cross-sectional scanning thermal microscopy. *Adv. Mater. Interfaces* **10**, 2300081 (2023).
14. D. Seto, R. Nikka, S. Nishio, Y. Taguchi, T. Saiki, Y. Nagasaka, Nanoscale optical thermometry using a time-correlated single-photon counting in an illumination-collection mode. *Appl. Phys. Lett.* **110**, 033109 (2017).
15. Q. Weng, K.-T. Lin, K. Yoshida, H. Nema, S. Komiyama, S. Kim, K. Hirakawa, Y. Kajihara, Near-field radiative nanothermal imaging of nonuniform Joule heating in narrow metal wires. *Nano Lett.* **18**, 4220–4225 (2018).
16. P.-I. Wang, Y. P. Zhao, G. C. Wang, T. M. Lu, Novel growth mechanism of single crystalline Cu nanorods by electron beam irradiation. *Nanotechnology* **15**, 218–222 (2004).
17. L. Shi, L. He, L. Shangguan, Y. Zhou, B. Wang, L. Zhang, Y. Yang, C. Teng, L. Sun, Revealing the phase segregation and evolution dynamics in binary nanoalloys via electron beam-assisted ultrafast heating and cooling. *ACS Nano* **16**, 921–929 (2022).
18. H. Guo, M. I. Khan, C. Cheng, W. Fan, C. Dames, J. Wu, A. M. Minor, Vanadium dioxide nanowire-based microthermometer for quantitative evaluation of electron beam heating. *Nat. Commun.* **5**, 4986 (2014).
19. M. Mecklenburg, A. H. William, E. R. White, R. Dhall, B. C. Stephen, S. Aloni, B. C. Regan, Nanoscale temperature mapping in operating microelectronic devices. *Science* **347**, 629–632 (2015).
20. X. Yan, C. Liu, C. A. Gadre, S. Dai, L. Gu, K. Yu, T. Aoki, R. Wu, X. Pan, Unexpected strong thermally induced phonon energy shift for mapping local temperature. *Nano Lett.* **19**, 7494–7502 (2019).
21. M. J. Lagos, P. E. Batson, Thermometry with subnanometer resolution in the electron microscope using the principle of detailed balancing. *Nano Lett.* **18**, 4556–4563 (2018).
22. J. C. Idrobo, A. R. Lupini, T. Feng, R. R. Unocic, F. S. Walden, D. S. Gardiner, T. C. Lovejoy, N. Dellby, S. T. Pantelides, O. L. Krivanek, Temperature measurement by a nanoscale electron probe using energy gain and loss spectroscopy. *Phys. Rev. Lett.* **120**, 095901 (2018).
23. N. Kawamoto, Y. Kakefuda, T. Mori, K. Hirose, M. Mitome, Y. Bando, D. Golberg, Visualizing nanoscale heat pathways. *Nano Energy* **52**, 323–328 (2018).
24. N. Kawamoto, Y. Kakefuda, I. Yamada, J. Yuan, K. Hasegawa, K. Kimoto, T. Hara, M. Mitome, Y. Bando, T. Mori, D. Golberg, Nanoscale characterization of the thermal interface resistance of a heat-sink composite material by *in situ* TEM. *Nanotechnology* **26**, 465705 (2015).
25. D. R. Lide, Section 4 in *CRC Handbook of Chemistry and Physics*, 85th Edition (CRC Press, 2004), p. 4–39.
26. Y. S. Touloukian, R. W. Powell, C. Y. Ho, P. G. Klemens, *Thermophysical Properties of Matter Vol 2 Thermal Conductivity Nonmetallic Solids* (IFI/Plenum, 1970), p. 94–97.
27. Y. S. Touloukian, E. H. Buyco, *Thermophysical properties of matter Vol 5 Specific Heat: Nonmetallic Solids* (IFI/Plenum, 1970), pp. 26–29.
28. Y. Hu, L. Zeng, A. J. Minnich, M. S. Dresselhaus, G. Chen, Spectral mapping of thermal conductivity through nanoscale ballistic transport. *Nat. Nanotechnol.* **10**, 701–706 (2015).
29. D. G. Cahill, W. K. Ford, K. E. Goodson, G. D. Mahan, A. Majumdar, H. J. Maris, R. Merlin, S. R. Phillpot, Nanoscale thermal transport. *J. Appl. Phys.* **93**, 793–818 (2002).

30. A. J. Minnich, J. A. Johnson, A. J. Schmidt, K. Esfarjani, M. S. Dresselhaus, K. A. Nelson, G. Chen, Thermal conductivity spectroscopy technique to measure phonon mean free paths. *Phys. Rev. Lett.* **107**, 095901 (2011).
31. A. J. Minnich, Determining phonon mean free paths from observations of quasiballistic thermal transport. *Phys. Rev. Lett.* **109**, 205901 (2012).
32. C. Hua, A. J. Minnich, Transport regimes in quasiballistic heat conduction. *Phys. Rev. B* **89**, 094302 (2014).
33. P. Torres, M. Royo, M. López-Suárez, J. Shiomi, R. Rurali, Quasiballistic phonon transport from first principles. *Phys. Rev. B* **102**, 144305 (2020).
34. Y. D. Wilde, F. Formanek, R. Carminati, B. Gralak, P.-A. Lemoine, K. Joulain, J.-P. Mulet, Y. Chen, J.-J. Greffet, Thermal radiation scanning tunnelling microscopy. *Nature* **444**, 740–743 (2006).
35. M. J. Lagos, A. Trügler, U. Hohenester, P. E. Batson, Mapping vibrational surface and bulk modes in a single nanocube. *Nature* **543**, 529–532 (2017).
36. Y. Wu, J. Ordonez-Miranda, S. Gluchko, R. Anufriev, D. D. S. Meneses, L. D. Campo, S. Volz, M. Nomura, Enhanced thermal conduction by surface phonon-polaritons. *Sci. Adv.* **6**, eabb4461 (2020).
37. L. Tranchant, S. Hamamura, J. Ordonez-Miranda, T. Yabuki, A. Vega-Flick, F. Cervantes-Alvarez, J. J. Alvarado-Gil, S. Volz, K. Miyazaki, Two-dimensional phonon polariton heat transport. *Nano Lett.* **19**, 6924–6930 (2019).
38. W. Kim, Strategies for engineering phonon transport in thermoelectrics. *J. Mater. Chem. C.* **3**, 10336–10348 (2015).
39. A. T. Wieg, Y. Kodera, Z. Wang, C. Dames, J. E. Garay, Thermomechanical properties of rare-earth-doped AlN for laser gain media: The role of grain boundaries and grain size. *Acta Mater.* **86**, 148–156 (2015).
40. X. Wu, L. Tang, C. L. Hardin, C. Dames, Y. Kodera, J. E. Garay, Thermal conductivity and management in laser gain materials: A nano/microstructural perspective. *J. Appl. Phys.* **131**, 020902 (2022).
41. P. K. Kuo, G. W. Auner, Z. L. Wu, Microstructure and thermal conductivity of epitaxial AlN thin films. *Thin Solid Films* **253**, 223–227 (1994).
42. Y. Zhao, C. Zhu, S. Wang, J. Z. Tian, D. J. Yang, C. K. Chen, H. Cheng, P. Hing, Pulsed photothermal reflectance measurement of the thermal conductivity of sputtered aluminum nitride thin films. *J. Appl. Phys.* **96**, 4563–4568 (2004).
43. C. Duquenne, M. P. Besland, P. Y. Tessier, E. Gautron, Y. Scudeller, D. Averty, Thermal conductivity of aluminium nitride thin films prepared by reactive magnetron sputtering. *J. Phys. D* **45**, 015301 (2012).
44. R. L. Xu, M. M. Rojo, S. M. Islam, A. Sood, B. Vareskic, A. Katre, N. Mingo, K. E. Goodson, H. G. Xing, D. Jena, E. Pop, Thermal conductivity of crystalline AlN and the influence of atomic-scale defects. *J. Appl. Phys.* **126**, 185105 (2019).
45. G. Chen, Non-Fourier phonon heat conduction at the microscale and nanoscale. *Nat. Rev. Phys.* **3**, 555–569 (2021).
46. G. Wehmeyer, Modeling ballistic phonon transport from a cylindrical electron beam heat source. *J. Appl. Phys.* **126**, 124306 (2019).
47. K. L. Chopra, S. K. Bahl, M. R. Randlett, Thermopower in thin-film copper—Constantan couples. *J. Appl. Phys.* **39**, 1525–1528 (1968).
48. G. P. Szakmany, A. O. Orlov, G. H. Bernstein, W. Porod, Single-metal nanoscale thermocouples. *IEEE Trans. Nanotechnol.* **13**, 1234–1239 (2014).
49. M. C. Salvadori, A. R. Vaz, F. S. Teixeira, M. Cattani, I. G. Brown, Thermoelectric effect in very thin film Pt/Au thermocouples. *Appl. Phys. Lett.* **88**, 133106 (2006).
50. L. Scarioni, E. M. Castro, Thermoelectric power in thin film Fe–CuNi alloy (type-J) couples. *J. Appl. Phys.* **87**, 4337–4339 (2000).
51. N. W. Ashcroft, N. D. Mermin, Chapter 2 in *Solid State Physics* (Harcourt College, 1976), p. 52.
52. A. J. Angström, XVII. New method of determining the thermal conductibility of bodies. *Science* **25**, 130–142 (1863).
53. J. Morikawa, T. Hashimoto, Analysis of high-order harmonics of temperature wave for Fourier transform thermal analysis. *Jpn. J. Appl. Phys.* **37**, L1484 (1998).
54. L. Reimer, Chapter 10 in *Transmission Electron Microscopy* (Springer-Verlag, ed. 3, 1993), p. 435–438.
55. H. Meltzman, Y. Kauffmann, P. Thangadurai, M. Drozdov, M. Baram, D. Brandon, W. D. Kaplan, An experimental method for calibration of the plasmon mean free path. *J. Microsc.* **236**, 165–173 (2009).
56. Y. Kakefuda, N. Kawamoto, M. Mitome, I. Yamada, T. Mori, D. Golberg, Development of nanoscale thermocouple probes for local thermal measurements. *Surf. Sci. Nanotechnol.* **17**, 102–107 (2019).
57. A. A. Mohtar, G. Tessier, R. Ritasalo, M. Matvejeff, J. Stormonth-Darling, P. S. Dobson, P. O. Chapuis, S. Gomès, J. P. Roger, Thickness-dependent thermal properties of amorphous insulating thin films measured by photoreflectance microscopy. *Thin Solid Films* **642**, 157–162 (2017).
58. A. Salazar, A. Sánchez-Lavega, J. M. Terrón, Effective thermal diffusivity of layered materials measured by modulated photothermal techniques. *J. Appl. Phys.* **84**, 3031–3041 (1998).

Acknowledgments: We thank A. Takahashi and M. Oishi for support of the FIB fabrication. H.D.N. and N.K. thank O. Cretu for the fruitful discussion and support of image analysis using DigitalMicrograph software. H.D.N. is grateful to T. D. Ngo for supporting the Python script for mapping analysis and calculation. **Funding:** This work was supported by JST-Mirai Program (grant no. JPMJM19A1), Japan Society for the Promotion of Science (grant nos. JP 20H02093 and 22F22367), Australian Research Council (ARC) (grant FL160100089), and Advanced Research Infrastructure for Materials and Nanotechnology in Japan (ARIM) of the Ministry of Education, Culture, Sports, Science and Technology (MEXT) with the proposal number JPMXP1223NM5265. **Author contributions:** Conceptualization: H.D.N., I.Y., N.K., D.G., and K.K. Methodology: I.Y, N.K., H.P., and D.G. Investigation: H.D.N., H.P., I.Y., N.K., H.C., and D.G. Visualization: H.D.N., I.Y, N.K., and D.G. Funding acquisition: H.D.N., T.M., D.G., and N.K. Project administration: H.D.N., N.K., D.G., H.C., and K.K. Resource: T.N. Supervision: N.K., H.D.N., T.M., D.G., and K.K. Writing—original draft: H.D.N., N.K., and D.G. Writing—review and editing: H.D.N., D.-M.T., J.K., H.P., M.M., D.G., K.K., T.M., and N.K. **Competing interests:** There are three Japanese patent applications (application no. 2013-172783, patent no. 6164735, application no. 2023-80591, and application no. 2023-87455). Details of these applications are provided as follows: Application 1: Current patent status: Patent valid name of the organization issuing the patent: Japan Patent Office Names of related authors: N.K., T.M., D.G., and M.M.; dates: 2 March 2015 (release date); serial number: patent no. 6164735. Application 2: Current patent status: Patent pending name of the organization issuing the patent: Japan Patent Office Names of related authors: N.K., H.D.N., T.M., M.M., and K.K.; dates: 16 May 2023 (filing date); serial number: patent request no. 2023- 80591. Application 3: Current patent status: Patent pending name of the organization issuing the patent: Japan Patent Office Names of related authors: N.K., H.D.N, T.M., M.M., and K.K.; dates: 29 May 2023 (filing date); serial number: patent request no. 2023- 87455. The authors declare that they have no other competing interests. **Data and materials availability:** All data needed to evaluate the conclusions in the paper are present in the paper and/or the Supplementary Materials.

Submitted 23 June 2023
Accepted 15 December 2023
Published 12 January 2024
10.1126/sciadv.adj3825